A 4 x 4 x 416 digital SiPM array with 192 TDCs for multiple high-resolution timestamp acquisition



2013 JINST 8 P05024

(http://iopscience.iop.org/1748-0221/8/05/P05024)

PUBLISHED BY IOP PUBLISHING FOR SISSA MEDIALAB

RECEIVED: *January 7, 2013*
REVISED: *March 15, 2013*
ACCEPTED: *April 14, 2013*
PUBLISHED: *May 31, 2013*

2013 JINST 8 P05024

# A 4 × 4 × 416 digital SiPM array with 192 TDCs for multiple high-resolution timestamp acquisition

**S. Mandai**[1] **and E. Charbon**

*Faculty of Electrical Engineering, TU Delft,*
*Mekelweg 4, 2628 CD Delft, The Netherlands*

*E-mail:* s.mandai@tudelft.nl

ABSTRACT: We present a 4 × 4 array of digital silicon photomultipliers (D-SiPMs) capable of timestamping up to 48 photons per D-SiPM and we show the advantage of generating multiple timestamps in the context of positron emission tomography (PET). The D-SiPMs have a pitch of 800 µm and comprise 416 pixels each; the timing resolution achieved by the SiPMs is 179 ps FWHM, while each pixel has a fill factor of up to 57 % and a single-photon timing resolution of 114 ps.

KEYWORDS: Timing detectors; Photon detectors for UV, visible and IR photons (solid-state) (PIN diodes, APDs, Si-PMTs, G-APDs, CCDs, EBCCDs, EMCCDs etc); Pixelated detectors and associated VLSI electronics; Instrumentation and methods for time-of-flight (TOF) spectroscopy

[1]Corresponding author.



doi:10.1088/1748-0221/8/05/P05024

## Contents



2013 JINST 8 P05024

## 1 Introduction

Photomultiplier tubes (PMTs) are widely used for cancer diagnostics, such as Positron Emission Tomography (PET), scientific research and industrial instrumentation, such as spectrophotometry or Fluorescence-lifetime imaging microscopy (FLIM), and in high energy physics.

A Silicon photomultiplier (SiPM) is an alternative to PMTs; it is often preferred because of its tolerance to magnetic fields, compactness, and low bias voltage. At least two flavors exist for SiPMs: analog and digital. An analog SiPM (A-SiPM) consists of an array of avalanche photodiodes operating in Geiger mode, whose avalanche currents are summed in one node as shown in figure 1 (a) [1–6]. The resulting current is proportional to the number of detected photons, thus providing single- and multiple-photon detection capability. In a digital SiPM (D-SiPM), each photo-detecting cell or pixel consists of a single-photon avalanche diode (SPAD), specific circuit elements are added to generate digital signals for each photon detection and to turn off the SPAD when its activity is deemed too high (this SPAD is known as screamer [7]). All of the SPAD outputs are combined together by means of a digital OR; see figure 1 (b). In most D-SiPMs, the global output is directly routed to an on-chip time-to-digital converter (TDC) to reduce external components and temporal noise. Though, the time uncertainty for single-photon detection is limited by SPAD jitter and TDC non-linearities, as well as systematic skews due to imperfectly balanced routing. A-SiPMs are especially sensitive to these systematic skews, while in D-SiPMs they can be largely

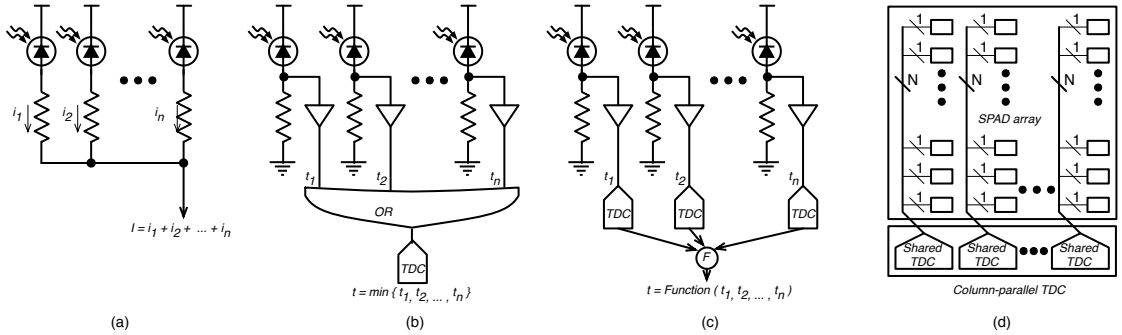


**Figure 1**. The concept of (a) Analog SiPM, (b) conventional Digital SiPM, (c) ideal digital SiPM and (d) Multi-channel Digital SiPM.

removed or compensated for. The disadvantage of D-SiPM is the fact that only one optical photon or noise event determines the response of the sensor. Alternatively, the approach pursued in [8] can achieve balanced routing by implementing a on-pixel TDC as shown in figure 1 (c). At the same time multiple photons can be detected independently, thus providing more detailed statistical information of the Gamma event in case of PET applications. However in this approach, the fill factor is low due to the use of a TDC per pixel. To increase fill factor while capturing multiple photon statistics, multiple pixels can share one TDC. Figure 1 (d) [15] shows a case in which a column of SPADs shares one TDC. The skew problem is also improved when compared to conventional D-SiPMs for single-photon detection, and the multiple-time information can be utilized in a statistical approach for multiple-photon detection [9, 10].

In this paper, we present a $4 \times 4$ Multi-channel Digital SiPM (MD-SiPM) coupled with 192 TDCs. The TDCs provide a detailed temporal map of the shower of photons resulting from a gamma-ray scintillation. Deriving the timestamp of the scintillation from the temporal map is a non-trivial process; details on the process can be found in [9, 10], and further analysis is presented in this paper to model the effects of noise and non-ideal fill factor. The authors also show the basic characterization of the proposed MD-SiPM.

The paper is organized as follows. Section 2 shows the analysis of the MD-SiPM using a statistical model for a PET application. In section 3, the architecture of the proposed SiPM is presented. Section 4 presents SiPM measurements, including photon detection efficiency (PDE), dark count rate (DCR) and timing resolution with an integrated TDC array. Finally, conclusions are given in section 5.

## 2 Analysis of MD-SiPM in case of PET application

Here we present the analysis of MD-SiPM in case of PET application [11].

### 2.1 Simulation model

For the emitted photons from a LYSO scintillator, we can assume that detection occurs at time, $\theta$. Time information of each photon can be considered as statistically independent and identically distributed (i.i.d.) following a probability density function (pdf), which has been modeled as a double-exponential with rise time $t_r$ and decay time $t_d$ [12] $f(t|\theta) = (\exp(-\frac{t-\theta}{t_d}) - \exp(-\frac{t-\theta}{t_r}))/(t_d - t_r)$



2013 JINST 8 P05024

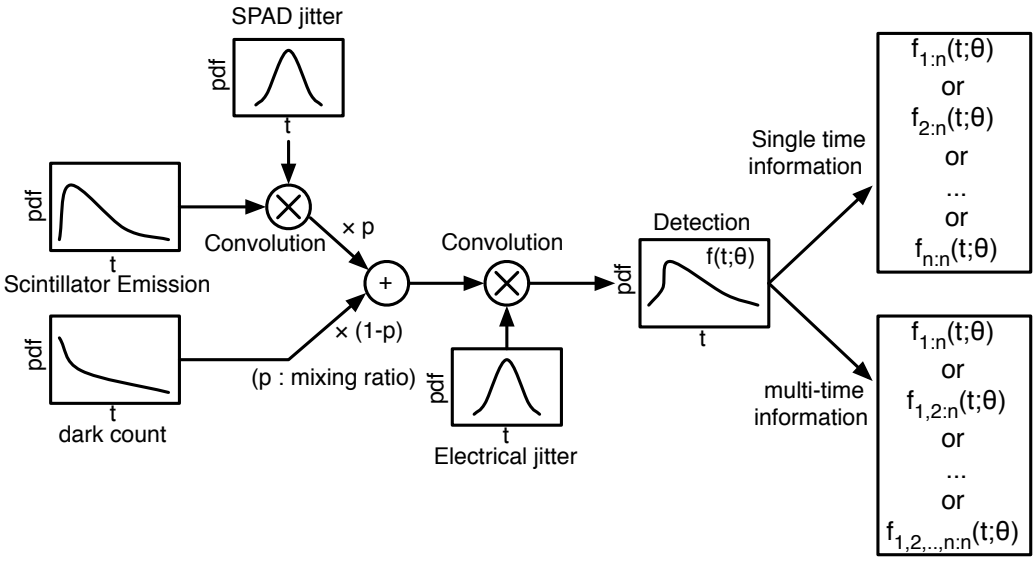


**Figure 2**. Method for calculating the probability distribution function of the emission from scintillator and DCR.

when t $> \theta$, otherwise, $f(t|\theta) = 0$. Upon photon impingement, the SPAD jitter and an electrical jitter are convolved with the scintillator-based pdf, $f_{emi}(t|\theta)$. The dark counts follow an exponential probability distribution with event rate, $\lambda$, and reset time, $t_r$, as $f(t) = \lambda \exp(-\lambda(t - t_r))$ when $t > t_r$, otherwise, $f(t) = 0$. The pdf of the dark counts should also be convolved with electrical jitter to be $f_{dcr}(t|t_r)$. The detection cycle, or frame, starts at the earliest before $\theta$ and it lasts a frame period, T. Thus the dark count pdf is summed up for each reset time and then normalized. The scintillator-based pdf and the dark count pdf are mixed with mixing ratio $\alpha : (1 - \alpha)$ where $\alpha$ is defined by the percentage of photons emitted from scintillator, N, out of total detectable events, $N + \lambda T$, as,

$$f_{emi+dcr}(t|\theta) = \alpha f_{emi}(t|\theta) + (1-\alpha)\frac{\int_{\theta-T}^{\theta} f_{dcr}(t|tr)\,dr}{\int_{\theta-T}^{\theta}\int_{t_r}^{\infty} f_{dcr}(t|tr)\,dt\,dr}.$$

Finally, the mixed pdf is used for calculating the Fisher information [13] for the rth-order statistics pdf or the joint pdf for the first r-order statistics, then the Crámer-Rao lower bound for the unbiased estimator, $\theta$, is calculated. This procedure is shown in figure 2.

### 2.2 Simulation results

For our simulations, we assumed normal SPAD jitter and electrical jitter distributions with a standard deviation of 100 ps, the rise and decay times of a LYSO scintillator are 200 ps and 40 ns, respectively, while the number of detected photons is varied from 100 to 5000, and DCR is varied from 1 Hz to 100 MHz. Figure 3 shows the relation between order statistics and full-width-at-half-max (FWHM) timing resolution. Figure 3 (a) shows that the timing resolution improves with multiple timestamps. Furthermore, the timing resolution with multiple timestamps doesn't degrade due to DCR while the timing resolution with a single timestamp degrades with certain amount of DCR, as shown in figure 3 (b). The FWHM with multiple timestamps improves 13% if compared



2013 JINST 8 P05024

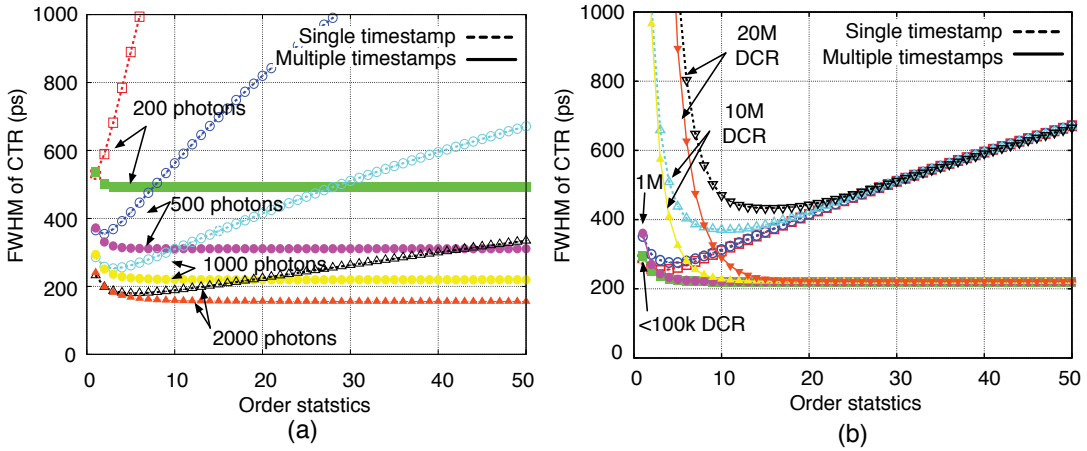


**Figure 3**. Order statistics with a single timestamp or multiple timestamps v.s. FWHM of timing resolution: (a) various number of detected photons, 200, 500, 1000, and 2000 at 1 Hz DCR (which is almost negligible), (b) various values of DCR, less than 1 MHz, 10 MHz, 20 MHz at 1000 detected photons.

to the FWHM with a single timestamp at less than 100 kHz DCR, however, the FWHM is 20% and 40% better at 1 MHz and 10 MHz DCR, respectively. From this work, it is clear that D-SiPMs capable of providing multiple timestamps are useful not only to improve timing resolution but especially to ensure tolerance to DCR and independence from a threshold. The proposed MD-SiPM is considered to be a promising architecture, as it achieves a good trade-off between detection robustness and timing resolution, thanks to a high overall fill factor.

## 3 Proposed SiPM architecture

### 3.1 SiPM configuration

Figure 4 shows the proposed MD-SiPM array configuration. Each SiPM in the array comprises 416 photo-detecting cells and measures 800 $\times$ 780 $\mu m^2$, adapted to the crystal dimensions. A 20 µm gap enables adequate glue reflow in the pixelation process. Each pixel measures 50 µm $\times$ 30 µm; it generates a sharp pulse in correspondence to a photon detection that is routed directly to a TDC. Adjacent pixels are routed to independent TDCs by triples (every three pixel, the TDC is reused); this approach prevents closely striking photons to be missed, thereby reducing local saturation. There are 48 TDCs per SiPM column, each operating simultaneously with a LSB duration of 44 ps. The number of photons, and thus the energy of the gamma event, is proportional to the number of triggered pixels. Thus, after each event the triggered pixels are counted; the corresponding digital code (1 or 0) is read out along with the complete statistical profiles of the projected photons, and summed up to calculate the total number of photons in one SiPM. Even though the number of cells is 416, it is possible to utilize the saturation correction to count more than the number of cells [14]. To minimize photon misses, the array was designed with a fill factor up to 57%. In our application, the pitch of the SiPMs is 800 µm, so as to match the 800 $\times$ 800 $\mu m^2$ section of the individual crystal in a pixelated scintillator; vertically there is a 20 µm gap to allow for glue reflow. So the overall fill factor is equivalent to the fill factor of one pixel. To minimize dark



2013 JINST 8 P05024

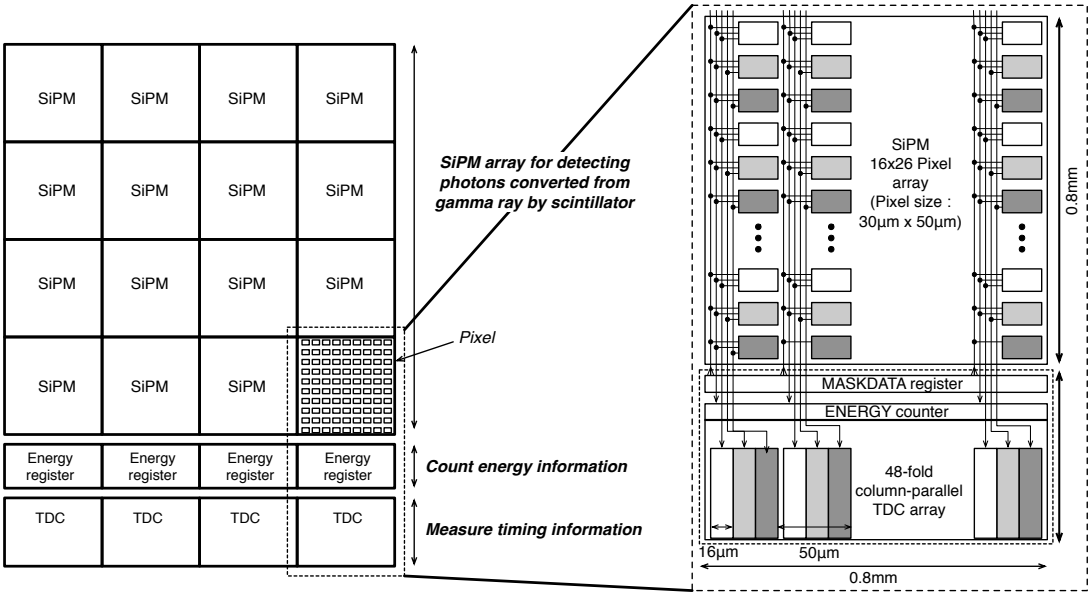


**Figure 4**. Block diagram of the proposed sensor capable of detecting a large number of photons and their time-of-arrival with picosecond accuracy. The large number of TDCs enables to construct an accurate statistical profile for gamma photons.

counts in a SiPM, a masking procedure is used. Masking an SiPM consists of depriving it from a certain number of screamers. The MASKDATA register is used for disabling those pixels with DCR exceeding a threshold, so as to minimize spurious TDC activation. The ENERGY register is used for reading out the number of pixels that detected at least a photon.

### 3.2 Pixel architecture

Figure 5 (a) shows the schematic of a pixel; it comprises the SPAD, a 1-bit counter for energy estimation, a masking circuit, and a pulse shaper / column driver. The frame will start after RST reset the SPAD. When a shower of photons is generated in the scintillator, one of them may hit the SPAD in the pixel, generating a digital pulse to pull-down TIMING$_m$. QBIAS controls the quenching resistance of the SPAD and controls the digital pulse width to be more than the frame period. The event triggers the 1-bit counter, and it is read out as ENERGY$_m$ by ROW after latching the 1-bit counter value by SET. Masking is carried out in advance row-by-row, using signals MASKDATA$_m$ and ROWCALSEL, by bringing the SPAD bias below breakdown and by disabling the signal generated at its anode.

Figure 5 (b) shows the schematic of the pre-charge circuit of each TDC. This circuit is used to prepare a TDC for a photon hit by GRST. TIMING$_m$ is pre-charged during RST for pixels and TDCs that occurs periodically every 6 μs via signal GRST. PCLK is also causing RST for pixels and TDCs when the number of firing TDCs exceeds a threshold within a pre-determined time, say 100 ns. This premature reset, known as *smart reset* is performed so as to prevent misses when TDCs are occupied by background photons or noise. VPRE is used for pull-up resistance for TIMING$_m$, and TIMING$_m$ will be used as START for TDC.



2013 JINST 8 P05024

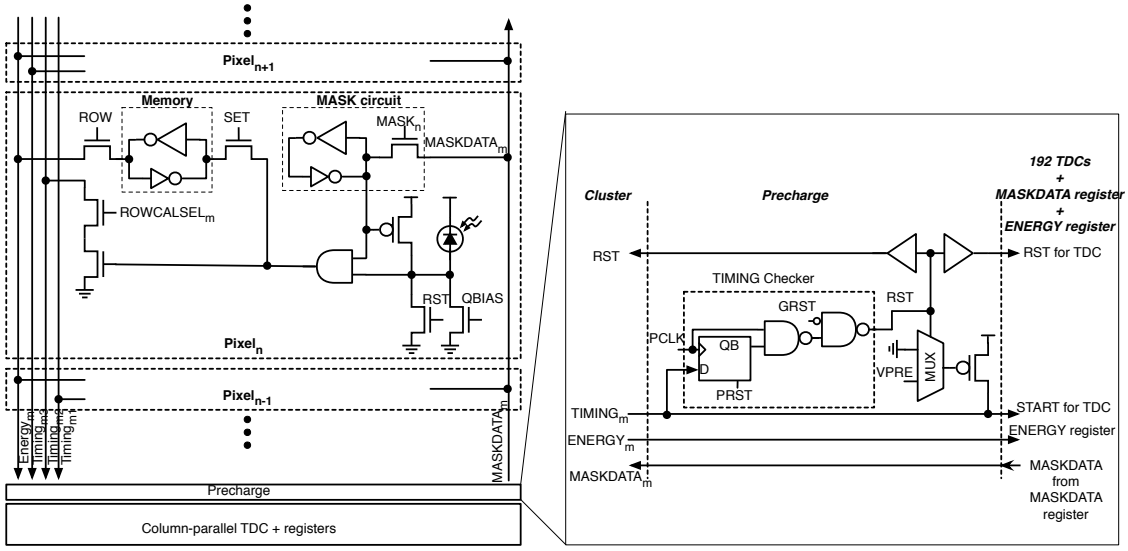


**Figure 5**. (a) The pixel architecture comprises a SPAD, a 1-bit counter for energy estimation, a memory for masking, active and passive quenching, and a column driver circuit. (b) Detail of the pre-charge structure implemented at the bottom of the array.

### 3.3 Column-parallel TDC

There are 192 TDCs in one single row outside the SiPM array. A voltage-controlled oscillator (VCO) generates and distributes 4 differential phases to all the TDCs, as shown in figure 6 (a). The phases, with 45 degree difference, are delivered from the VCO to all TDCs, and each TDC generates a clock (CLK) synchronized to the VCO frequency that is delivered to a 12-bit counter. Figure 6 (b) shows one TDC performing a coarse conversion and a fine conversion, subsequently. The coarse conversion is achieved by counting the clock cycles from the assertion of START (SPAD firing on the corresponding column) to the end of the frame (STOP signal) using the 12-bit counter; the LSB of this conversion is 1.4 ns. In the fine conversion, upon START assertion, the phases from the VCO are latched by two-phase detectors with slightly skewed signals, $ENB_1$ and $ENB_2$. The small skew is realized by implementing two different inverter chains biased differently and calibrated to have a optimized skew for best DNL. The phase detectors employ an interpolation technique to double the phase resolution. Conventionally, the phase detectors locate the timing of $ENB_1$ and $ENB_2$ within $\phi$<0> and $\bar{\phi}$<0>, $\phi$<1> and $\bar{\phi}$<1>, $\phi$<2> and $\bar{\phi}$<2>, and $\phi$<3> and $\bar{\phi}$<3> using comparators. By expanding the comparison to $\phi$<0> and $\bar{\phi}$<3>, $\phi$<0> and $\bar{\phi}$<1>, $\phi$<1> and $\bar{\phi}$<2>, and $\phi$<2> and $\bar{\phi}$<3>, the interpolated phase is also detectable [15]. The extra circuit elements are only four comparators and a memory, while the TDC can be smaller compared to the literature [16]. Figure 6 (c) shows the VCO schematic; the VCO is activated at the beginning of the frame by enabling the ring oscillation and stopped at the end of the frame to save power. Figure 6 (d) shows the bandgap voltage reference circuit for the VCO and the inverter chain in the TDC to ensure stable frequency generation and delay control on chip. The VCO frequency and delay of the inverter chain in the TDC may also be conveniently programmed. Figure 6 (e) shows the timing diagram showing the TDC operation. Two 4-bit phase information, $PHVAL_1$ and



2013 JINST 8 P05024

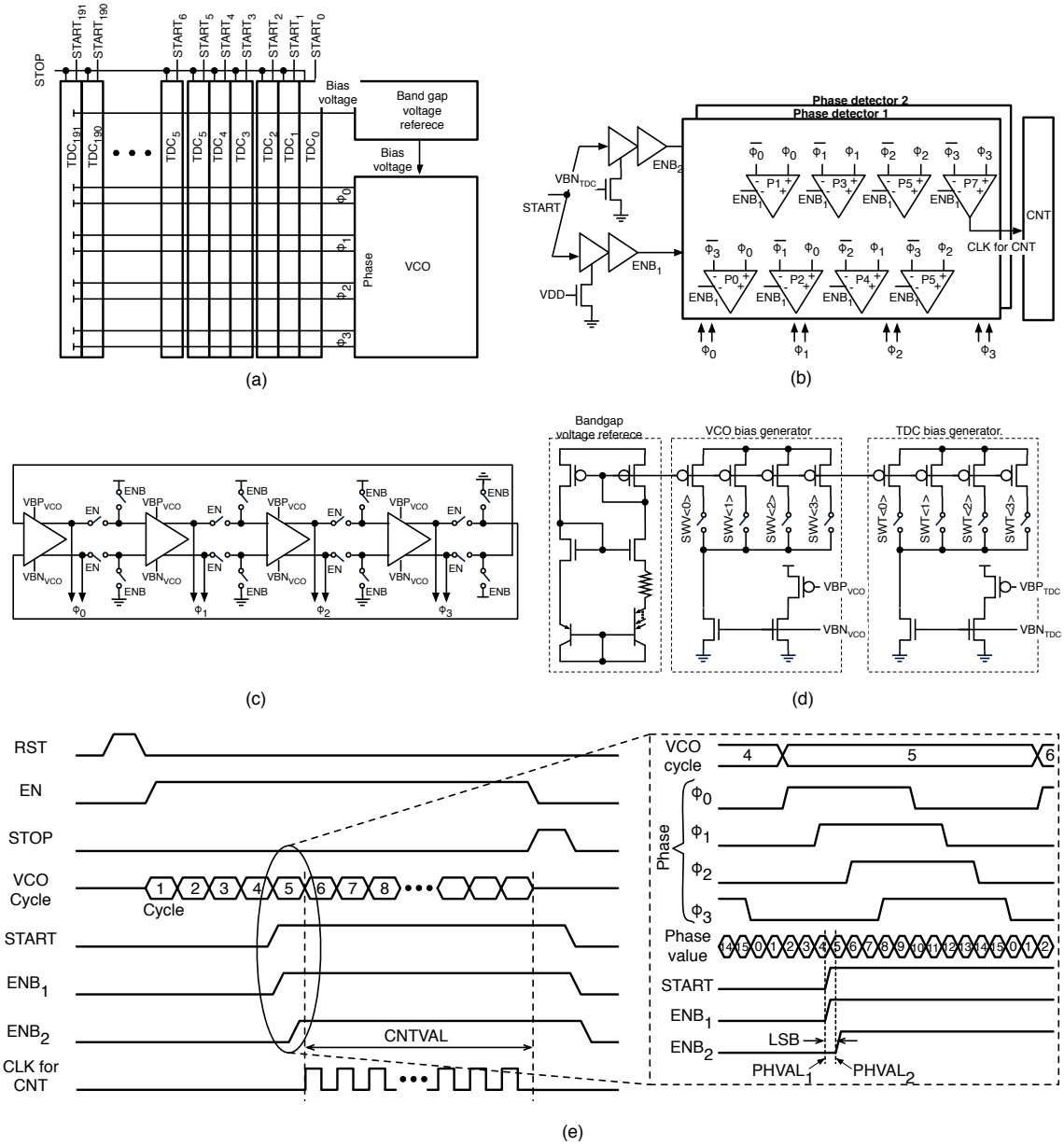


**Figure 6**. (a) VCO and reference circuit distributing 4 differential high-frequency phases to 192 TDCs. (b) Schematic of each TDC employing the phase interpolation technique. (c) VCO. (d) Bandgap voltage reference circuit. (e) Timing diagram.

$PHVAL_2$, are latched by $ENB_1$ and $ENB_2$, and CNTVAL is stored as a coarse conversion result. By summing $PHVAL_1$ and $PHVAL_2$, we obtain a fine conversion resolution of 5 bits (corresponding to a LSB of $1.4\ \text{ns}/2^5 = 44$ ps), which, added to the 12 bits of the coarse conversion, corresponds to a total of 17 bits. The final code is calculated as below,

$$Code = CNTVAL \times 32 + (PHVAL_1 + PHVAL_2)\,.$$



2013 JINST 8 P05024

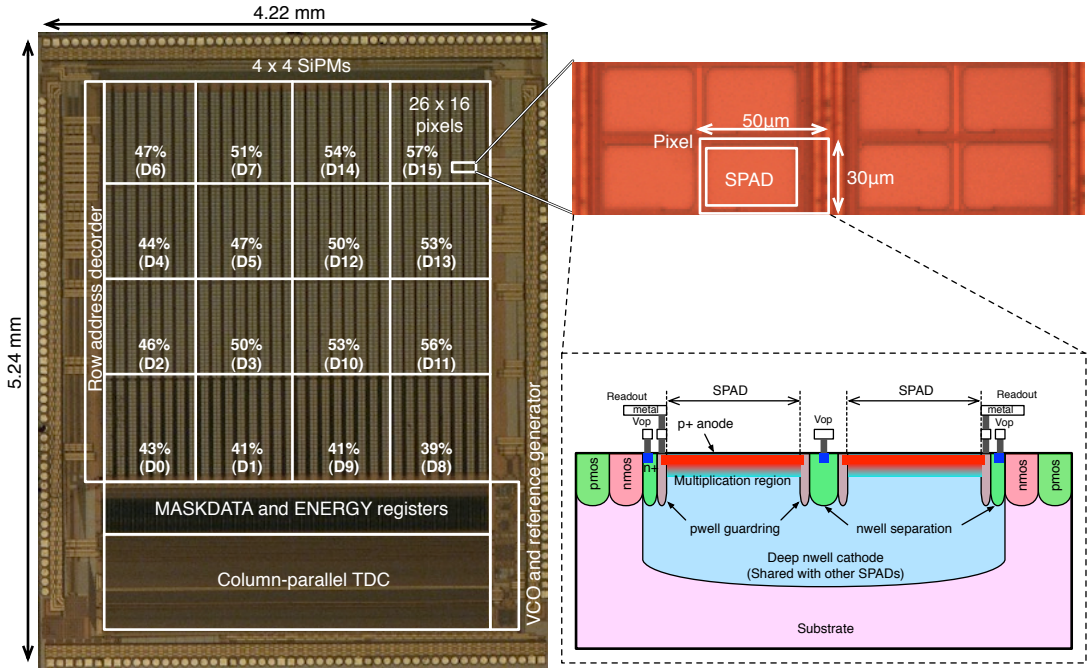


**Figure 7**. Chip microphotograph. The chip occupies an area of 22.1 mm$^2$ with a sensitive area of 3.2 × 3.2 mm$^2$. The cross-section and a detail of the pixels are also shown.

## 4 Measurement results

### 4.1 Chip fabrication

The sensor chip was fabricated on a 0.35 µm CMOS process, the die size is 4.22 × 5.24 mm$^2$. The 4 × 4 MD-SiPM array occupies 3.2 × 3.2 mm$^2$ and each TDC occupies 16 × 840 µm$^2$ including the readout circuit. The power supply voltage is 3.3 V and the high voltage for SPADs is 22−23V. The VCO and the bandgap voltage reference consume 80 mA in total, the digital logic 30 mA. The current drawn by each TDC is less than 570 µA, while the MD-SiPM array consumption is 2 mA in the dark.

Figure 7 shows the chip microphotograph, which includes an array of 4 × 4 MD-SiPMs, a row address decoder, MASKDATA and ENERGY registers, and a row of 192 TDCs. An independent SiPM readout (not shown in the picture) was implemented for testing purposes. Each SiPM and its fill factor are shown in the figure, along with a denomination used in section 4. A detail of the SiPM 'D15' is shown in the figure, along with the dimensions of the pixel that achieves a fill factor of 57%. To maximize fill factor, the electronics was placed at a distance of twice the pitch and implemented in a mirrored fashion. The cross-section and a detail of the SPADs, whereby deep well sharing was extensively used in the cathode.

### 4.2 Noise and sensitivity characterization

Figure 8 (a) shows the cumulative DCR plot for 'D15' SiPM showing the DCR distribution of 416 SPADs for several excess bias voltages and temperatures. The photon detection probability (PDP) of SPADs is also characterized with a lamp, a monochrometer (Oriel/Newport part 77250) and an



2013 JINST 8 P05024

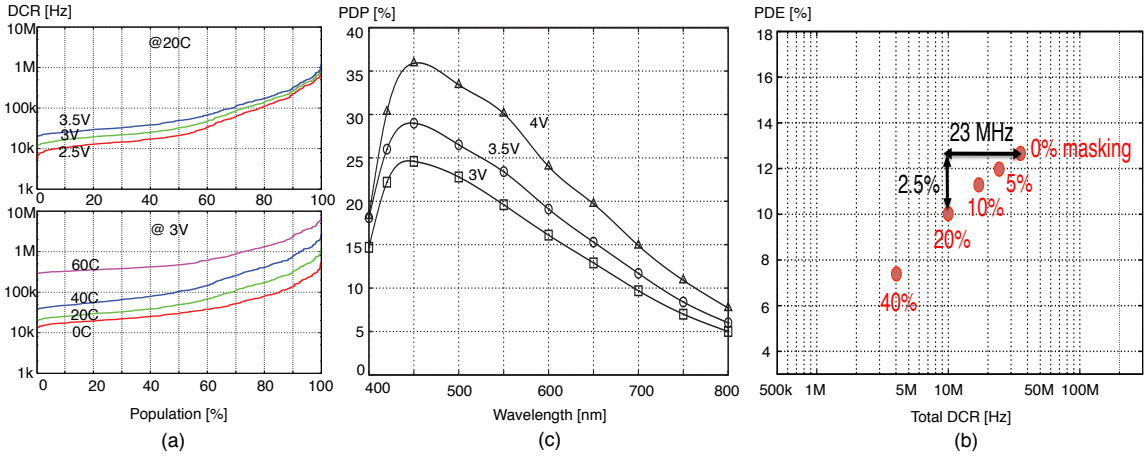


**Figure 8**. (a) Cumulative DCR plot for various excess bias voltage and temperature conditions for the 'D15' SiPM. (b) PDP v.s. wavelength at various excess bias. (c) Relation between DCR and PDE for various SiPMs at 3 V excess bias and 20 °C for several masking levels.

integration sphere (Oriel/Newport part 819D-SL-2) attaching our detector and a reference photodiode (Hamamatsu part S1226-BQ). When PDP is measured, afterpulsing and cross-talk should be negligible not to overestimate PDP. We only activate a single SPAD to measure PDP and the dead time of the SPAD is set to be long by using high quenching resistor. Figure 8 (b) shows PDP of a single pixel as a function of wavelength with different excess bias. The temperature dependency of PDP is negligible in the spectral range of interest. PDP is about 30 % at 4 V excess bias at 420–430 nm which is of interest for TOF PET applications with LYSO scintillators. It means that at most 17.1 % PDE can be achievable by accepting the extremely high DCR or cooling the device. PDE can be calculated based on the PDP measurement results and fill factor by $PDP \times FF$, where $FF$ the fill factor. Masking pixels reduces both DCR and fill factor, and thus PDE. However, the reduction is not linear because some pixels have very high DCR compared to the median DCR value. Thus, small masking levels reduce total DCR in one SiPM faster than PDE, while larger masking has a larger impact on PDE and a smaller impact on total DCR. This mechanism for 'D15' at 3 V excess bias and 20 C can be seen in figure 8 (c).

### 4.3 Timing characterization

The TDCs were fully characterized using an electrical input, yielding a single-shot timing uncertainty of 60 ps (FWHM). Figure 9 (a) and (b) show DNL and INL of a typical TDC in the TDC array, and figure 9 (c) shows the INL variation for all 192 TDCs after INL compensation which is based on look-up table. Figure 9 (d) shows the LSB shift of the TDCs due to temperature and power supply fluctuations. The TDCs suffer from a 6 % to 9 % LSB shift in the $\pm 30$ °C range and $\pm$ 10 % power supply variation.

The timing resolution of each SiPM was established optically in a TCSPC experiment using a 250 mW, 405 nm laser source (ALDS GmBH) with 40 ps pulse width and an external oscilloscope (LeCroy WaveMaster 6200). The TCSPC experiment was repeated using the internal TDCs operating at a nominal LSB of 44 ps. A single-SPAD timing jitter (FWHM) of 114 ps was measured



2013 JINST 8 P05024

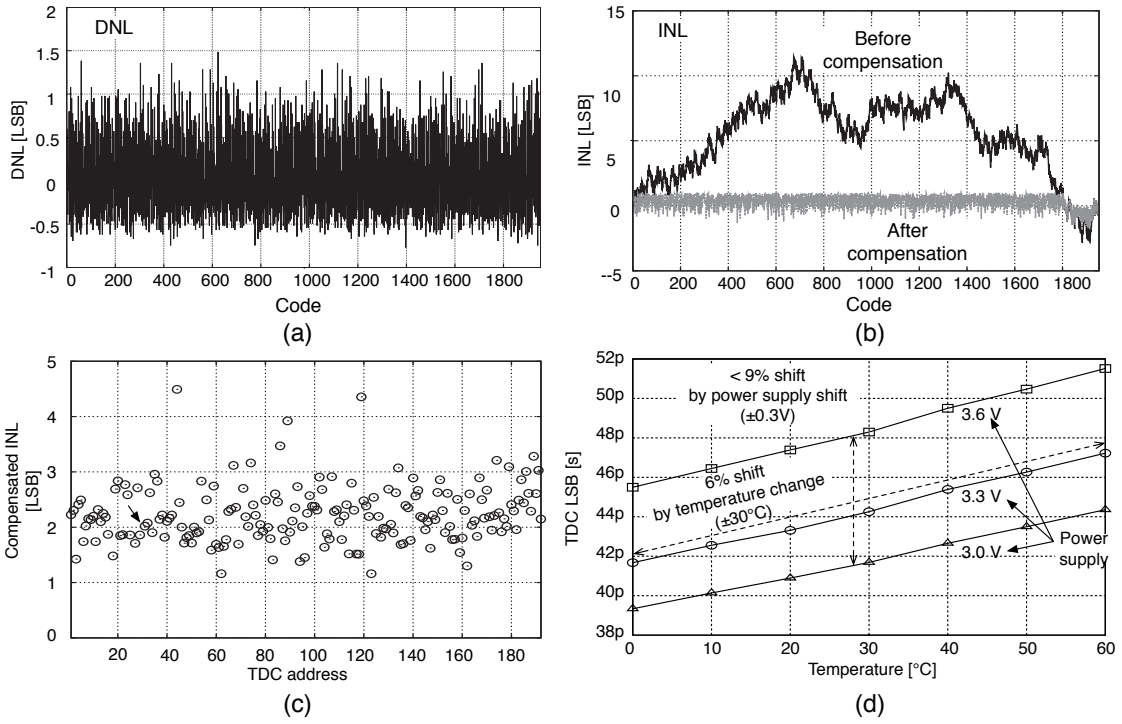


**Figure 9**. (a) DNL. (b) INL. (c) INL variation after compensation in a TDC when all 192 TDCs are in operation. (d) LSB shift for the TDC due to temperature and power supply fluctuation.

with internal TDCs and confirmed by the oscilloscope, as illustrated in figure 10 (a). The timing jitter of the entire SiPM (all 416 pixels) was measured using the internal TDCs, yielding a single-shot timing jitter as low as 179 ps (FWHM) at 3.0V excess bias, as shown in figure 10 (b). This measurement is the sum in quadrature of the contributions from the intrinsic jitter of the SPADs, TDCs, and sensor skews.

Table 11 summarizes the 4 $\times$4 MD-SiPM specifications in relation with conventional SiPMs. The major advantage of our sensor over conventional SiPMs with comparable fill factor is the flexibility and robustness given by the capability to establish multiple timestamps. This is especially important, considering the extreme environments in which the sensor is designed to operate.

### 4.4 Coincident timing resolution prediction

To predict the coincident timing resolution (CTR) based on the MD-SiPM architecture and measurement data shown in the previous subsections, we carried out another simulation. For the simulations, the timing jitter for a single photon of the detector is swept from 50 ps to 1 ns while the parameters of a LYSO scintillator are the same as in section 2. Figure 12 (a) shows the relation between the timing information for a single photon and the predicted FWHM of CTR with various number of detected photons at negligible DCR level. According to the simulation results, the predicted CTR for the MD-SiPMs with 179 ps single photon timing jitter will be 260 ps and 183 ps for 500 and 1000 photons respectively by utilizing multiple timestamps figure 12 (b) shows the relation between the timing information for a single photon and the predicted FWHM of CTR with various DCR values at 1000 detected photons. As shown in the results, CTR utilizing multiple timestamps



2013 JINST 8 P05024

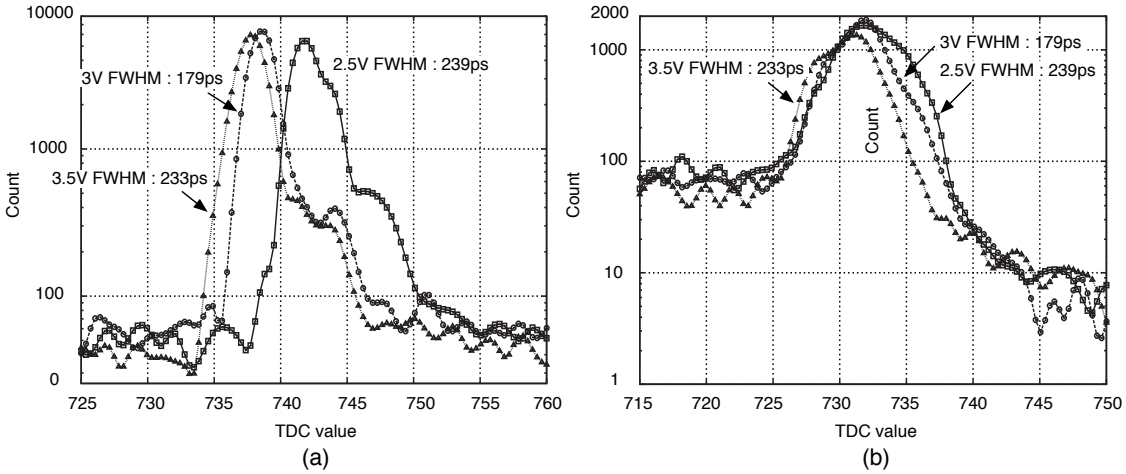


**Figure 10**. (a) Single-photon FWHM timing resolution for a single SPAD using a TDC and an external oscilloscope. (b) Single-photon FWHM timing resolution for the complete SiPM at various excess bias voltages.

| Parameter | | This work | [5] | [6] | [7] | [8] |
|---|---|---|---|---|---|---|
| Chip | Technology | 0.35 μm CMOS | Custom | Custom | 0.18 μm CMOS | 0.13 μm CMOS |
| | # SiPMs | 4 x 4 | 1 | 1 | 1 | 1 |
| | # SPAD / SiPM | 416 | 1600/400/100 | 4900 | 6400 | 20480 |
| | SiPM Area | 800μm×780μm | 1mm×1mm | 3.5mm×3.5mm | 3.8mm×3.3mm | 8mm×6.4mm |
| TDC | # TDCs / SiPM column | 48 | Analog SiPM No TDCs | Analog SiPM No TDCs | 2 | 20480 |
| | # total TDC | 192 | | | 2 | 20480 |
| | Power / TDC (mA) | 0.57uA | | | - | - |
| | TDC LSB | 44 | | | 24ps | 55ps |
| SPAD | DCR (Hz/μm² @ 20℃) | 39 @ Ve=3.0V | 1.95/1.3/1.27 | 2.08 | 0.19 | 2 @ Ve=0.73V |
| | PDP at 420 nm (%) | 30 @ Ve=4.0V | - | - | ~60 | 22.5 @ Ve=1.7V |
| | Jitter (ps) | 114 @ 405 nm | - | - | - | 140 @ 637 nm |
| | FF (%) | 57 (D15) | - | - | 50 | 1 |
| SiPM | FF (%) | 55.6<br>39.1* | 30.8/61.5/78.5 | 36 | 50 | 1 |
| | Maximum PDE (%) | 17 (D15) | 25/50/65 | - | 15 | - |
| | Total DCR (MHz) | 10 (20℃, 20% mask) | 0.6/0.8/1 | 0.75 | ~2 (20C,5%mask) | - |
| | Cross-talk (%) | < 10 | Included in PDE | - | 1 | - |
| | Noisy pixels(%) | < 30 | - | - | 5 | - |
| | Power [mW] | 330 (16 SiPMs) | - | - | -- | 550 |
| | Timing resolution for blue light (single photon) (ps) | 179 @ Ve=3.0V | 200-300 | 164 @ Ve=5.0V | > 350** | 280 |

* Including TDC arrays and readout circuit assuming all SiPMs are D15
** According authors' measurement and prediction

**Figure 11**. Specification summary and comparison table. All the measurements are at room temperature unless otherwise specified.

doesn't degrade due to DCR while CTR utilizing a single timestamp degrades with certain value of DCR.



2013 JINST 8 P05024

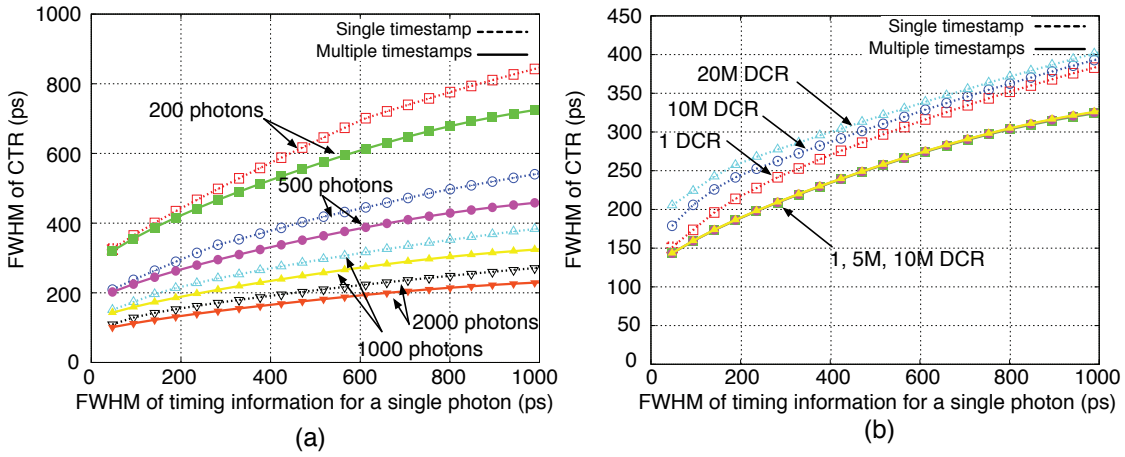


**Figure 12**. Timing information for a single photon v.s. predicted FWHM of timing resolution (CTR) with a single timestamp and multiple timestamps: (a) various number of detected photons, 200, 500, 1000, and 2000 at 1 Hz DCR (which is almost negligible), (b) various values of DCR, 1 Hz, 5 MHz, 10 MHz at 1000 detected photons.

## 5 Conclusion

We have presented the statistical analysis of timing resolution of a D-SiPM including the effect of PDE, DCR and electrical jitter when multiple timestamps are available in PET applications, and show that D-SiPMs utilizing multiple timestamps (Multi-channel D-SiPM or MD- SiPM) can be more tolerant to DCR than those utilizing a single timestamp. We also present the implementation of $4 \times 4$ MD-SiPMs coupled with 44ps LSB, 192 TDCs. The pitch of the SiPMs is 800 µm and the number of pixels in one SiPM is 416. The maximum pixel fill factor is 57 % with 114 ps timing resolution for a single photon detection. The SiPM timing resolution for a single photon is 179 ps FWHM.

## Acknowledgments

The research leading to these results has received funding from the European Union Seventh Framework Programme (FP7/ 2007-2013) under Grant Agreement n°256984. The authors would like to thank Vishwas Jain of TU Delft and Pierre Jarron of CERN. The authors are also grateful to Xilinx, Inc. for FPGA donations.

## References

[1] P. Buzhan et al., *Silicon photomultiplier and its possible applications*, *Nucl. Instrum. Meth.* **A 504** (2003) 48.

[2] A.G. Stewart, V. Saveliev, S.J. Bellis, D.J. Herbert, P.J. Hughes and J.C. Jackson, *Performance of 1-mm2 silicon phopomultiplier*, *IEEE J. Quantum Electron.* **44** (2008) 157.

[3] N. Zorzi, M. Melchiorri, A. Piazza, C. Piemonte and A. Tarolli, *Development of large-area silicon photomultiplier detectors for PET applications at FBK*, *Nucl. Instrum. Meth.* **A 636** (2010) 208.



2013 JINST 8 P05024

[4] M. McClish et al., *Performance measurements of CMOS position sensitive solid-state photomultipliers*, *IEEE Trans. Nucl. Sci.* **57** (2010) 2280–2286.

[5] MPPC, http://jp.hamamatsu.com.

[6] M. Mazzillo et al., *Timing performances of large area silicon photomultipliers fabricated at STMicroelectronics*, *IEEE Trans. Nuc. Sci.* **57** (2010) 2273.

[7] T. Frach, G. Prescher, C. Degenhardt, R. de Gruyter, A. Schmitz, and R. Ballizany, *The digital silicon photomultiplier — Principle of operation and intrinsic detector performance*, *IEEE Nucl. Sci. Symp. Conf. Rec.* **N28–5** (2009).

[8] C. Veerappan et al., *A 160×128 single-photon image sensor with on-pixel 55ps 10b time-to-digital converter*, *IEEE ISSCC Dig. Tech. Papers* (2011) 312.

[9] M.W. Fishburn and E. Charbon, *System trade-offs in gamma-ray detection utilizing SPAD arrays and scintillators*, *IEEE Trans. Nuc. Sci.* **57** (2010) 2549.

[10] S. Seifert, H.T. van Dam and D.R. Schaart, *The lower bound on the timing resolution of scintillation detectors*, *Phys. Med. Biol.* **57** (2012) 1797.

[11] S. Mandai and E. Charbon, *A Multi-Channel Digital SiPMs: Concept, Analysis and Implementation*, *IEEE Nucl. Sci. Symp. Conf. Rec.* **N34–4** (2012).

[12] J. Glodo et al., *Effects of ce concentration on scintillation properties of labr3:ce*, *IEEE Trans. Nucl. Sci.* **52** 2005 1805.

[13] S. Park, *On the asymptotic fisher information in order statistics*, *IMetrika* **57** 2003 71.

[14] C. Degenhardt et al., *The Digital Silicon Photomultiplier ? A Novel Sensor for the Detection of Scintillation Light*, *IEEE Nucl. Sci. Symp. Conf. Rec.* (2009) 2383.

[15] S. Mandai and E. Charbon, *A Fully-Integrated 780 × 800 $\mu m^2$ Multi-Digital Silicon Photomultiplier With Column-parallel Time-to-Digital Converter*, *in Proc. IEEE ESSCIRC* (2012) 89.

[16] S. Mandai and E. Charbon, *A 128-Channel, 8.9-ps LSB, Column-Parallel Two-Stage TDC Based on Time Difference Amplification for Time-Resolved Imaging*, *IEEE Trans. Nucl. Sci.* **59** (2012) 2463.

2013 JINST 8 P05024